

A NOVEL HYBRID METHOD FOR HELICOPTER COST EFFECTIVE AEROELASTIC SIMULATIONS

Giorgos Papadakis, Dimitris Manolas, Vasilis A Riziotis, Spyros G Voutsinas
School of Mechanical Engineering, National Technical University of Athens, GR15780, Athens, Greece

Abstract

Aiming at increasing the fidelity of aeroelastic simulations for helicopter configurations without excessively penalizing the computational cost, a novel hybrid flow solver is proposed. The widely used domain decomposition technique is given a different twist by also differentiating the method used in the sub-domains. The proposed solver combines grid based CFD with particle methods. To every blade a confined CFD grid is defined with an extent of ~ 1 chord. To this set-up a background flow is added defined in particle form. The formulation is compressible and so particles carry mass, vorticity, dilatation and pressure. A two-ways coupling of the two solvers is implemented. The background flow is used in providing the outer boundary conditions of the CFD grids while the CFD solution is used in order to update the information carried by particles that are contained in the CFD grids. For the aeroelastic simulations a multi-body structural solver is used. The blades are considered slender Timoshenko beam structures. Geometrical non-linearities are accounted for by subdividing every blade into sub-bodies that are subsequently treated separately while the equilibrium equations are implicitly formulated with respect to the coupling with flow through an iterative flow-to-structure interaction. The present work includes the description of the methodology and representative results taken from the HeliNoVi data base.

Key words: particle methods, aeroelastic coupling, Eulerian Lagrangian coupling, hybrid CFD

1 INTRODUCTION

It is widely recognized that high fidelity simulations are needed in order to advance the current understanding of the complex flow induced interactions that appear on helicopters. At research level, high fidelity in modeling has been achieved by coupling CFD (Computational Fluid Dynamics) with CSD (Computational Structural Dynamics). However high fidelity comes along with high cost which can become a bottleneck to a productive use of advanced modeling. This explains why primarily CFD is always in search of methods that reduce cost without compromising accuracy. In this regard, domain decomposition is a commonly used technique [1] which has significantly reduced the user time of CFD simulations. In standard domain decomposition, the same formulation is used in all sub-domains which is not always optimal. At increasing distances from solid boundaries, the grid becomes coarser which increases numerical diffusion. Furthermore, far field conditions are necessarily applied at finite distances which in some cases makes it necessary to introduce vortex corrections. In this respect, Lagrangian (Particle) methods have several advantages. They are grid-free and self-adaptive, having (in theory) zero numerical diffusion; domain truncation is not needed and the far field conditions are exactly embedded in the formulation [2], [3]. However, in particle methods wall boundary conditions constitute a major challenge, involving costly convolution operations and large number of particles [4], [5].

Therefore, since particle methods appear so complementary to Eulerian CFD, it is natural to combine the two in one single package following a domain decomposition approach.

Such a hybrid approach by the name HoPFlow, has been recently developed at NTUA [6] and is here adapted to helicopter applications. HoPFlow combines conventional grid based CFD with particle (Lagrangian) methods. For the CFD part, the in-house developed MaPFlow solver is used while for the Lagrangian part the incompressible vortex particle code GenUVP [7] is adapted. MaPFlow is a multi-block, MPI enabled, unstructured finite volume compressible URANS solver for deformable grids with pre-conditioning for low Mach numbers, and equipped with the $k-\omega$ SST turbulence model.

The CFD grid is confined around the solid boundaries and may be composed of more than one disjoint sub-domains (one per solid component). In this way, the wall conditions can be accurately imposed. By limiting the extent of the CFD subdomains, their outer boundaries are no longer in the far field and become interfaces on which the complete flow information is needed. This is provided by a background flow field defined in particle form. Particles carry mass, dilatation, vorticity and pressure and cover the entire flow domain. By overlapping the CFD and particle domains, the communication of flow information can be consistently defined. The coupling of the two solutions is strong and is established through an

iterative process carried out in every time step. In order to achieve the highest possible saving, the Particle Mesh method is used combined with Fast Poisson Solvers [8]. In addition to that, by confining the CFD grid, faster convergence is achieved since the balance with the outer boundary condition is done at significantly smaller distances from the solid boundaries and by that the overall cost drops substantially [9].

In the present paper, pure aerodynamic and aeroelastic simulations for the BO105 helicopter are presented and compared to the HeliNoVi experimental data base. Structural dynamics is included by coupling HoPFlow with the hGAST code [9] which is based on the multi-body approach and considers the blades as flexible Timoshenko beams. Geometrical non-linear effects introduced by large displacements and rotations are taken into account by splitting every component into smaller sub-bodies [9]. In this way, the deflections of previous sub-bodies are accumulated and introduced as rigid body motions to the next sub-body. Strong aeroelastic coupling is implemented by converging the coupled equations at every time step.

Fully coupled aeroelastic simulations have been reported in the past in contexts of varying complexity including that based on CFD-CSD coupling. The novelty of the present contribution is mainly on the cost required. The hybrid approach here presented differs from previous formulations of the same type [10],[11] in the following aspects: the conditions at the interfaces include the full flow information and not only vorticity; the coupling is strong; and the coupling does not require the solution of expensive integral equations at the interfaces. Furthermore, the present contribution assesses the capabilities of hybrid modeling in terms of cost effectiveness and accuracy which will eventually open its range of applicability to other problems as for example that concerning noise. In this respect minimizing numerical diffusion is of particular importance.

2 FORMULATION OF THE METHOD

2.1 The flow solver

The proposed methodology combines conventional grid based CFD with particle (Lagrangian) methods. In HoPFlow the CFD grid is confined around the solid boundaries and may be composed of more than one disjoint sub-domains (one per solid component). In this way, all solid boundaries are associated to the CFD part of the solver which can efficiently impose

the appropriate conditions. The CFD subdomains also need outer boundary conditions which are no longer in the far field. They are interfaces on which the complete flow information is needed. This is provided by a background flow field defined in particle form. Particles carry mass, dilatation, vorticity and pressure and cover the entire flow domain and thus overlap with the CFD domains. Such an overlapping allows the communication of the flow information from the CFD solution to the Particles. To ensure continuity and compatibility of the CFD and the particle solution a strong coupling between the two is imposed through an iterative process.

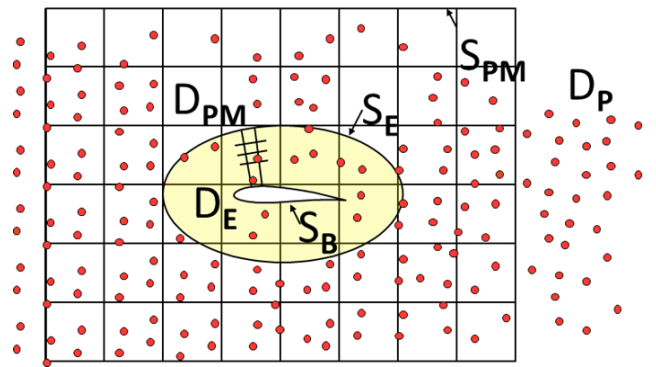


Figure 1. The domain decomposition

2.1.1 The Lagrangian part

Every particle is associated to a volume $V_p(t)$, centered at $\mathbf{Z}_p(t)$ and carries mass M_p , dilatation $\Theta_p(t)$, vorticity $\mathbf{\Omega}_p(t)$ and pressure $\Pi_p(t)$ collectively denoted by $\mathcal{Q}_p = \{M, \Theta, \mathbf{\Omega}, \Pi\}_p$;

$$(1) \quad \mathcal{Q}_p = \int_{V_p(t)} q(\mathbf{x}, t) dV_p(t) = q_p(t) V_p(t)$$

in which, $q(\mathbf{x}, t)$ denotes any of $\rho(\mathbf{x}, t)$, $\theta(\mathbf{x}, t)$, $\boldsymbol{\omega}(\mathbf{x}, t)$, $p(\mathbf{x}, t)$. The above volume averaging is combined with a smooth volume distribution also known as cut-off function. When the Particle Mesh (PM) technique is adapted, this role is taken over by the projection / interpolation function that passes the flow information from the particle positions to the PM grid nodes and vice-versa. Let $\mathcal{Q}_p = q_p \cdot V_p$ denote any flow quantity carried by the particles. Then for q_I at node I ,

$$(2) \quad q_I \equiv Proj_I(q_p; V_p) = \frac{\sum_p q_p V_p W(\mathbf{x}_I - \mathbf{Z}_p)}{\sum_p V_p W(\mathbf{x}_I - \mathbf{Z}_p)}$$

where \mathbf{x}_I denotes the position of the $I = i, j, k$ grid node, $W(\vec{r}) = W_1(r_x/h)W_1(r_y/h)W_1(r_z/h)$, h denotes the grid spacing, $\mathbf{r} = (r_x, r_y, r_z) = \mathbf{x}_I - \mathbf{Z}_p$ and W_1 the 1D interpolation function which is used. In the present work, the M_4' interpolation function is used which conserves the moments up to 3rd order (for other options see [2]). Any quantity defined on the grid, can be interpolated back to the particles positions using the same interpolation function:

$$(3) \quad q_p \equiv Interp_p(q_I) = \sum_I q_I W(\mathbf{x}_I - \mathbf{Z}_p)$$

The above approximations are introduced in the Lagrangian flow equations that are solved with a Runge-Kutta time marching scheme:

$$(4) \quad \begin{aligned} \frac{D\mathbf{Z}_p}{Dt} &= \mathbf{u}_p, & \frac{DV_p}{Dt} &= V_p \theta_p, & \frac{DM_p}{Dt} &= 0 \\ \frac{D\boldsymbol{\Omega}_p}{Dt} &= V_p \left((\boldsymbol{\omega} \cdot \nabla) \mathbf{u} - \frac{1}{\rho^2} \nabla \rho \times \nabla(-p + \boldsymbol{\sigma}) \right)_p \\ \frac{D\Theta_p}{Dt} &= V_p \left(2 \|\nabla \mathbf{u}\| + \nabla \cdot \left(\frac{\nabla(-p + \boldsymbol{\sigma})}{\rho} \right) \right)_p \\ \frac{D\Pi_p}{Dt} &= V_p \left((1 - \gamma) p \theta + (\gamma - 1) \nabla(\mathbf{u}\boldsymbol{\sigma}) \right)_p \end{aligned}$$

where D/Dt denotes the material time derivative, $(\cdot)_p$ indicates evaluation at the particle position \mathbf{Z}_p and $\boldsymbol{\sigma}$ denotes the viscous stress tensor.

The above system is supplemented with the Helmholtz velocity decomposition which splits the velocity field in two parts: an irrotational (curl free) defined by the scalar potential φ and a solenoidal one (divergence free) defined by the vector potential $\boldsymbol{\Psi}$ (also known as stream function):

$$(5) \quad \mathbf{u} = \mathbf{U}_\infty + \mathbf{u}_\varphi + \mathbf{u}_\omega, \quad \mathbf{u}_\varphi = \nabla\varphi, \quad \mathbf{u}_\omega = \nabla \times \boldsymbol{\Psi}$$

In which both potentials satisfy a Poisson equation:

$$(6) \quad \nabla^2 \varphi = \theta, \quad \nabla^2 \boldsymbol{\Psi} = -\boldsymbol{\omega}$$

leading to the following convolution expression:

$$(7) \quad \mathbf{u}(\mathbf{x}) = \vec{U}_\infty + \int_D (\theta(\mathbf{y}) \cdot + \boldsymbol{\omega}(\mathbf{y}) \times) \nabla G(\mathbf{r}) dD(\mathbf{y}) +$$

$$\int_S (\mathbf{n} \cdot \mathbf{u}(\mathbf{y}) \cdot + (\mathbf{n} \times \mathbf{u}(\mathbf{y})) \times) \nabla G(\mathbf{r}) dS(\mathbf{y})$$

where $G(r)$ denotes the Green function and $\mathbf{r} = \mathbf{x} - \mathbf{y}$. In (7) $\mathbf{n} \cdot \mathbf{u}$ and $\mathbf{n} \times \mathbf{u}$ correspond to the normal and tangential disturbance velocity components on S . It is important to note that θdD , $\mathbf{n} \cdot \mathbf{u} dS$ as well as $\boldsymbol{\omega} dD$, $(\mathbf{n} \times \mathbf{u}) dS$ are associated to the same kernel and hence they can be regarded respectively as singular (surface) dilatation θ_s and vorticity $\boldsymbol{\omega}_s$ and subsequently treated as particles without distinction.

The presence of convolutions in (7) is known to increase the cost $\propto N^2$. Decisive cost reduction can be accomplished by using the Particle Mesh (PM) technique [12] especially when combined with multi-block Fast Poisson solvers [8]. In PM the equations for φ and $\boldsymbol{\Psi}$ are solved on a Cartesian grid, and subsequently the solution is interpolated at the particle positions. It is noted that interpolation does not only concern the velocity but also the right hand side of (4). Terms containing differentiation are first calculated at the grid nodes using finite differences and then interpolated.

Remarks:

1. In HoPFlow, the implementation of the PM technique makes use of the James Lackner algorithm [8] which was found to outperform all others options that were tested.
2. In order to remedy the gradual loss of regularity in the particle representation, remeshing is applied. This is similar to grid adaptation/ refinement used in CFD. It consists of interpolating the data known at the PM grid nodes, to regularly distributed positions. In the present implementation remeshing is carried out at the end of every time step and makes use of the same interpolation function \tilde{W} that was associated to (2) and (3).
3. The PM grid is by definition finite and therefore particles may exit depending on the duration of the simulation. Discarding these particles will violate the balance of momentum and by that the loads on the solid boundaries. So they must be retained. In case the main focus is on the loads as in the present case, the following simplifications are introduced: particles in D_p retain their vorticity but are convected by the free-stream velocity while dilatation that corresponds to outgoing acoustic waves is exponentially damped.

2.1.2 The coupling procedure

The coupling between the two solvers in HoPFlow is carried out in two ways: on one hand the particle information within the CFD grids is updated at every time step using the CFD solution and on the other the particle solution provides the outer boundary conditions needed in CFD. Aiming at ensuring that at the end of every time step, the two solutions match over D_E (except very close to solid boundaries), an iterative procedure is followed.

The updating of the particle information in D_E , is done in two steps. First the velocity \mathbf{u}_c at the grid cell centers, is differentiated to give θ, ω and then combined with ρ and p to get $q_c = \{\rho, \theta, \omega, p\}$. Next q_c is interpolated at regular positions in every CFD cell leading to a set of particles P_E . For this operation iso-parametric finite element approximations are used which also determine the associated volumes. The number of particles per CFD grid cell depends on its size with respect to that of the PM grid. It is important to assure full coverage of the PM grid and adequate spacial density of particles. In the cases so far considered, 4 and 8 particles per cell have been found adequate in 2D and 3D simulations respectively.

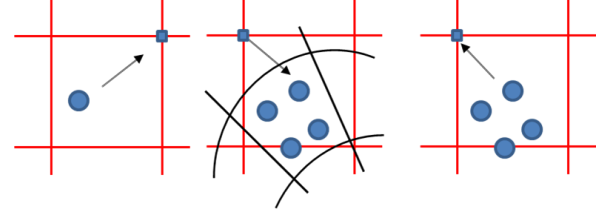
While the above correction is valid well within D_E , close to S_E there will be a projection error which is defined at the beginning of every time step. Let \hat{Q}_p denote the particle solution obtained by advancing in time the converged solution of the previous step. First \hat{Q}_p is projected to the PM grid nodes and \hat{q}_I is obtained. Then \hat{q}_I is interpolated at the P_E positions and finally back projected to the PM grid nodes (see Fig. 3).

$$(8) \quad error\{q_I\} = Proj_I\{Interp_{P_E}(\hat{q}_I)\}$$

The corrected solution is then readily defined by subtracting $error\{q_I\}$ from \hat{q}_I and adding q_E which is obtained from CFD,

$$(9) \quad q_I = \hat{q}_I - error\{q_I\} + q_E \quad q_E = Proj_I(q_{P_E}; V_E)$$

Once convergence between the two solvers is reached, q_I is transformed into particles.



$$\begin{aligned} \hat{Q}_p &= \hat{q}_p V_p & \hat{q}_I &= Proj_I\{\hat{q}_p, V_p\} \\ \hat{q}_E &= Interp_{P_E}\{\hat{q}_I\} & error\{q_I\} &= Proj_I\{\hat{q}_E, V_E\} \end{aligned}$$

Figure 2: Definition of $error\{q_I\}$.

2.2 The structural solver

In the present work, only the main rotor is simulated. The equilibrium equations (balance of forces and moments) are formulated in the context of the multi-body approach and solved with the Finite Element Method. Accordingly, every component is considered as a body undergoing rigid motions that are specified at the origin of its local system with respect to which elastic deflections are added. In order to synthesize the complete configuration, kinematic and dynamic continuity is imposed at all points connecting the components. In the present formulation, the components are divided into sub-bodies and therefore the need of imposing kinematic and dynamic continuity is extended to their connecting points.

The kinematic conditions are defined with respect to a set of displacements and rotations collectively denoted as $\mathbf{q} = \{q_n, n = 1, N_q\}$. A q_n can be one of the following: a pre-defined rigid motion (as the tilt angle and rotor speed); a control parameter (as the pitch setting), an existing degree of freedom (as the elastic displacements and rotations at the sub-body interconnections). In the third case a simple assignment equation is added to the system while in the second case the corresponding control equation. By considering all motions defined in \mathbf{q} as rigid body motions, the deformation along a component will gradually build up in a non-linear way. As explained next, another advantage is that linearization of the dynamic equations becomes straightforward which is important for defining an implicit solver.

An element q_n will either correspond to a translation or a rotation with respect to a space direction "dir_n". The first will define a displacement vector: $\mathbf{d}(q_n; dir_n)$ while the second a rotation matrix

$\mathbf{t}(q_n; \text{dir}_n)$. By defining specific sequences of rotations and translations the position \mathbf{r}_G of any point of the configuration can be expressed in global coordinates starting from its local position \mathbf{r}_L :

$$\mathbf{r}_G = \mathbf{d}_m + \mathbf{t}_m \cdot \left\{ \dots \left[\mathbf{d}_2 + \mathbf{t}_2 \cdot (\mathbf{d}_1 + \mathbf{t}_1 \cdot \mathbf{r}_L) \right] \right\} \Rightarrow$$

$$(10) \quad \mathbf{r}_G = \mathbf{R} + \mathbf{T} \cdot \mathbf{r}_L$$

$$\mathbf{R} = \mathbf{d}_m + \mathbf{t}_m \cdot \left\{ \dots \left[\mathbf{d}_2 + \mathbf{t}_2 \cdot \mathbf{d}_1 \right] \right\}, \mathbf{T} = \prod_{j=1}^m \mathbf{t}_j$$

In the above $\mathbf{r}_L = \mathbf{r}_{0L} + \mathbf{w}$ where \mathbf{r}_{0L} denotes the undeformed position and \mathbf{w} the elastic deformation given with respect to the elastic axis displacements and rotations. Note that with respect to \mathbf{q} the above expression is non-linear. Also because of this dependence \mathbf{R}, \mathbf{T} will vary in time.

With respect to the dynamic continuity at all connection points, the principle in the multi-body approach is that one of the connected bodies contributes displacements and rotations to all others, which in turn contribute their internal (reaction) loads. So, at the rotor center all blades contribute to the hub loads while the hub itself defines the kinematics. At the sub-body interconnections, the preceding sub-body provides the kinematics while the following one feeds back the reaction loads.

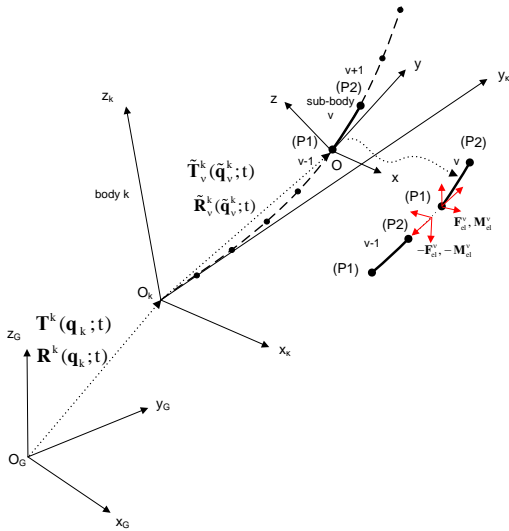


Figure 3: The sub-body concept.

2.2.1 Implementation of the sub-body concept

\mathbf{R}, \mathbf{T} operators are defined for every component “k” that position the local system $O_k x_k y_k z_k$ with respect

to the fixed system $O_G x_G y_G z_G$ (Figure 3). Such operators are also defined for every sub-body $v(k)$ with respect to the component local system $O_k x_k y_k z_k$ it belongs to. They are denoted as \mathbf{R}^k , \mathbf{T}^k and \mathbf{R}_v^k , \mathbf{T}_v^k respectively.

Based on the above it is possible to project the dynamic equations to the local directions with respect to which elastic deformations and aerodynamic loading are usually defined. Taking the acceleration as an example, the following expression at component level is obtained,

$$(11) \quad (\mathbf{T}^k)^T \cdot \ddot{\mathbf{r}}_G^k = \underbrace{(\mathbf{T}^k)^T \cdot \ddot{\mathbf{R}}^k}_{\text{acceleration of the origin}} + \underbrace{(\mathbf{T}^k)^T \cdot \ddot{\mathbf{T}}^k \cdot \mathbf{r}}_{\text{centrifugal acceleration}}$$

$$+ 2 \cdot \underbrace{(\mathbf{T}^k)^T \cdot \dot{\mathbf{A}}_k \cdot \dot{\mathbf{r}}_G^k}_{\text{Coriolis acceleration}} + \ddot{\mathbf{r}}^k$$

A similar expression is derived also at sub-body level.

Then as regards the linearization mentioned, by assuming small perturbations $\delta \mathbf{q}$ about a reference state \mathbf{q}^0 , \mathbf{q} and its time derivatives (velocity and acceleration), are approximated as:

$$(12) \quad \mathbf{q} = \mathbf{q}^0 + \delta \mathbf{q}, \dot{\mathbf{q}} = \dot{\mathbf{q}}^0 + \delta \dot{\mathbf{q}}, \ddot{\mathbf{q}} = \ddot{\mathbf{q}}^0 + \delta \ddot{\mathbf{q}}$$

and so

$$\mathbf{R}(\mathbf{q}) = \mathbf{R}(\mathbf{q}^0) + \partial_j \mathbf{R}(\mathbf{q}^0) \cdot \delta q_j$$

$$\dot{\mathbf{R}}(\mathbf{q}) = \partial_j \mathbf{R}(\mathbf{q}^0) \cdot \dot{q}_j^0 + \partial_{jk} \mathbf{R}(\mathbf{q}^0) \cdot \dot{q}_j^0 \cdot \delta q_k + \partial_j \mathbf{R}(\mathbf{q}^0) \cdot \delta \dot{q}_j$$

$$\ddot{\mathbf{R}}(\mathbf{q}) = \partial_j \mathbf{R}(\mathbf{q}^0) \ddot{q}_j^0 + \partial_{jk} \mathbf{R}(\mathbf{q}^0) \dot{q}_k^0 \dot{q}_j^0 +$$

$$\partial_{jkm} \mathbf{R}(\mathbf{q}^0) \dot{q}_k^0 \dot{q}_j^0 \delta q_m + \partial_{jk} \mathbf{R}(\mathbf{q}^0) \ddot{q}_j^0 \delta q_k +$$

$$2 \partial_{jk} \mathbf{R}(\mathbf{q}^0) \dot{q}_k^0 \delta \dot{q}_j + \partial_j \mathbf{R}(\mathbf{q}^0) \delta \ddot{q}_j$$

In the above expressions repeated indexes mean summation while $\partial_j(\cdot)$, $\partial_{jk}(\cdot)$, $\partial_{jkm}(\cdot)$ denote 1st, 2nd, 3rd derivative with respect to the corresponding q 's. Following a similar procedure, all non-linear terms in (11) can be linearized.

2.2.2 Aeroelastic coupling

Aeroelastic coupling includes two distinct interfaces. The first communicates the surface aerodynamic loads to the structure while the second updates the geometry and specifies the velocity at all points of the CFD grids. Let σ_F denotes the stress tensor of the fluid and \mathbf{n} the normal to the deformed solid boundary. The aerodynamic load is defined as $\sigma_F^T \mathbf{n}$. When a beam structural model is used, the aerodynamic loads must be integrated along the beam axis. Assuming that the relative position of a surface point with respect to the beam axis remains the same, $\sigma_F^T \mathbf{n}$ is first projected to the local coordinate system of the component (or corresponding sub-body) and then transferred to the beam axis. In doing that the moment of $\sigma_F^T \mathbf{n}$ must be included (for a straight blade the main moment component is the pitching one).

Then as regards the updating of the CFD grid kinematics, expression (10) is applied to all grid points. This operation always starts from the initial un-deformed position \mathbf{r}_{0L} and by that grid deformation is exact. By differentiating (10) in time the grid velocity is also obtained. It is noted that because the CFD grids have limited extent, their deformation will not risk of having line crossing that would lead to negative volumes. Furthermore, contrary to other grid deformation strategies the outer boundary will deform which is regarded as one of the advantages the specific hybrid solver has.

3 RESULTS

In the present work, simulations of the four-bladed BO105 rotor in forward flight at two different conditions are considered defined in Table 1. The specific values correspond to the values determined during the experimental campaign.

Case	U	Pitch	Roll	Col	Cos	Sin
1	32.8	1	0	5.9	1.9	-1.2
2	50.5	-2.6	2.8	7.2	1	-2.7

Table 1: Definition of test cases

Comparisons are made between the proposed solver (HoPFlow), the incompressible panel based vortex particle code (GenUVP) [7] and available experimental data [15] both sharing the same

structural solver. All simulations are considered inviscid.

For the GenUVP solver, a surface grid of 51x17 points covering the aerodynamic part of the blade (starting at $r/R=0.6$). For the HoPFlow solver, a grid of ~190k cells per blade has been defined that covered a volume around the blade surface of 1.5c width. These grids were embedded into a PM box covering the complete rotor area and the near part of the wake. In the present simulations, most of the wake was contained in the D_p part of the flow domain (see Figure 4).

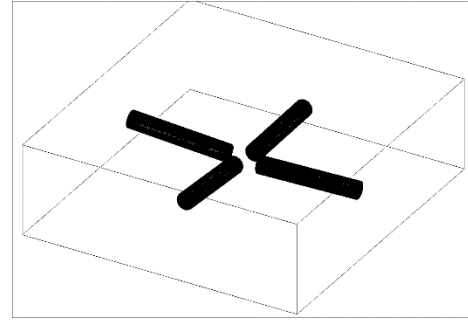


Figure 4: Overview of the computational set-up

In order to determine the numerical parameters for the two flow solvers, preliminary tests have been conducted. In the HoPFlow solver the PM spacing specifies the free-length that a particle is expected to cover within a time step and is therefore closely connected to the time step. On the other hand the time step is determined by the CFL condition of the CFD grids that are used. An indication was obtained from the Caradonna test cases [14]. In Figure 5 pure aerodynamic predictions obtained with HoPFlow and its full CFD version MaPFlow are compared to measured data. The case corresponds to hovering flight at local $Ma=0.877$. For a PM grid spacing of $0.2c$, good correlation in terms of pressure distributions has been obtained. At the specific stations shock waves appear that are correctly predicted both in position and intensity. Predictions of similar quality were obtained for all the Caradonna tests [14].

Next the case of a forward flight at 50.5m/s for the BO105 is considered which turned out to be significantly more challenging. Convergence in terms of the PM spacing is shown in Figure 6.

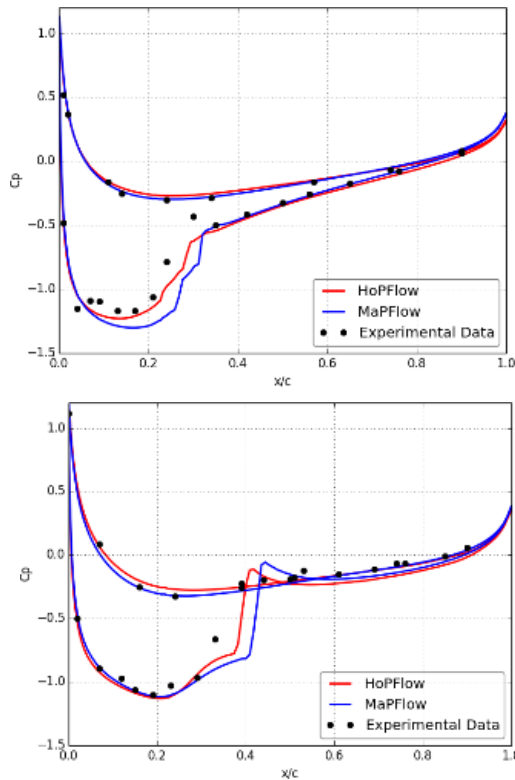


Figure 5: Pressure distributions at $r/R=87\%$, 95% . Case study: Caradonna rotor in hover at $Ma=0.877$

Results from spacing of 0.15 , 0.2 and $0.3c$ are compared all calculated with 480 steps per rotation. Over the advancing side the $0.2c$ spacing provides convergence for most of the blade length and certainly the lift producing part. This is clear at the 180deg azimuth position. On the contrary, over the retreating side, convergence is slower indicating the need for smaller spacing. The reason for that is the asymmetry of the loading conditions between the two sides that generates a significantly thicker wake over the retreating side where load balancing requires trimming to higher angles of attack

3.1 Aerodynamic simulations

In this section, purely aerodynamic results are presented for Cases 1 and 2. Instantaneous pressure distributions at 8 azimuth positions are shown in Fig 7,8 in which measured data are also included for comparison. The specific simulations use the trim given in Table 1 and do not include any account of the torsion that is by default present in the tests. Furthermore, the fuselage which was present in the tests is not included.

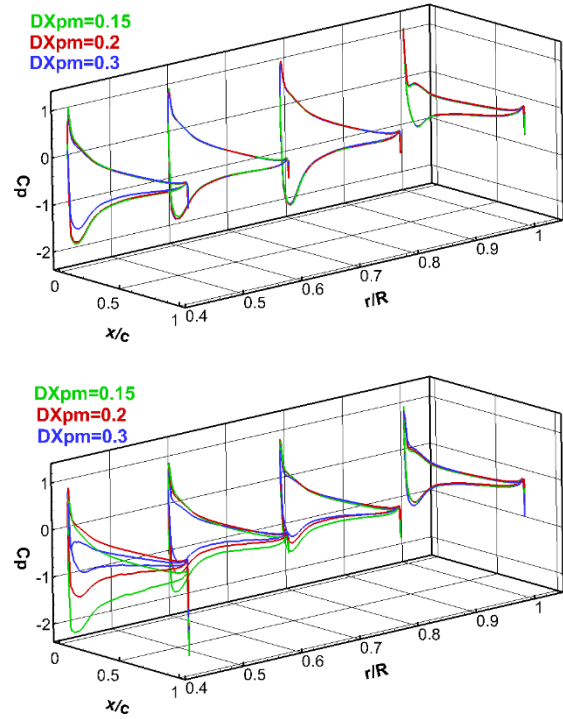


Figure 6: Convergence in terms of the PM spacing. The pressure distribution over the blade at 180 (upper) and 270deg of azimuth. Case study: forward flight at 50.5m/s

In Figure 7 and Figure 8 the pressure distributions at $r/R=0.87$ at 8 azimuth positions are depicted. The measured data are added to the plots as simple reference, since the response of the blade in torsion will change the aerodynamic conditions and therefore the pressure distributions will be different. In both flight conditions, the two simulations give overall similar behavior. At 90 and 120deg of azimuth HoPFlow predicts the formation of shock waves which GenUVP is not capable to predict by definition. It can be noted that the shocks appear more intense in the low speed case. This is due to the combined effect of rotor pitch attitude and blades pitching which in the low speed case lead to higher geometrical angle of attacks around the position of $\psi=90^\circ$ – rotor pitch is higher by 3.6° while lateral cyclic compensates the difference in the collective trim value. This is shown in Figure 9 that gives the variation of the angle of attack as estimated in the GenUVP simulations.

Besides the above the balancing of the pressure field over the disk is different. From $\psi=30^\circ$ up to $\psi=210^\circ$ the loading HoPFlow gives is higher than that of GenUVP. The opposite is noted over the rest of the

disk. In fact, the sector over which HoPFlow predicts lower loading corresponds to positions where the effect of the wake over the retreating side is expected to be more intense. As already mentioned, a PM spacing of $0.2c$ is not adequate. For the higher speed case results corresponding to PM spacing of $0.15c$ have been added. This increase in resolution mainly affects this sector directing the results to higher

loading. This is also clearly seen in the azimuth variation of the normal loading given in Figure 10.

Finally, in Figure 11 and Figure 12 the azimuth variation of the resulting main loads at blade root are given. In the 50.5m/s case the comparison between the two solvers is better than that seen in the lower speed case.

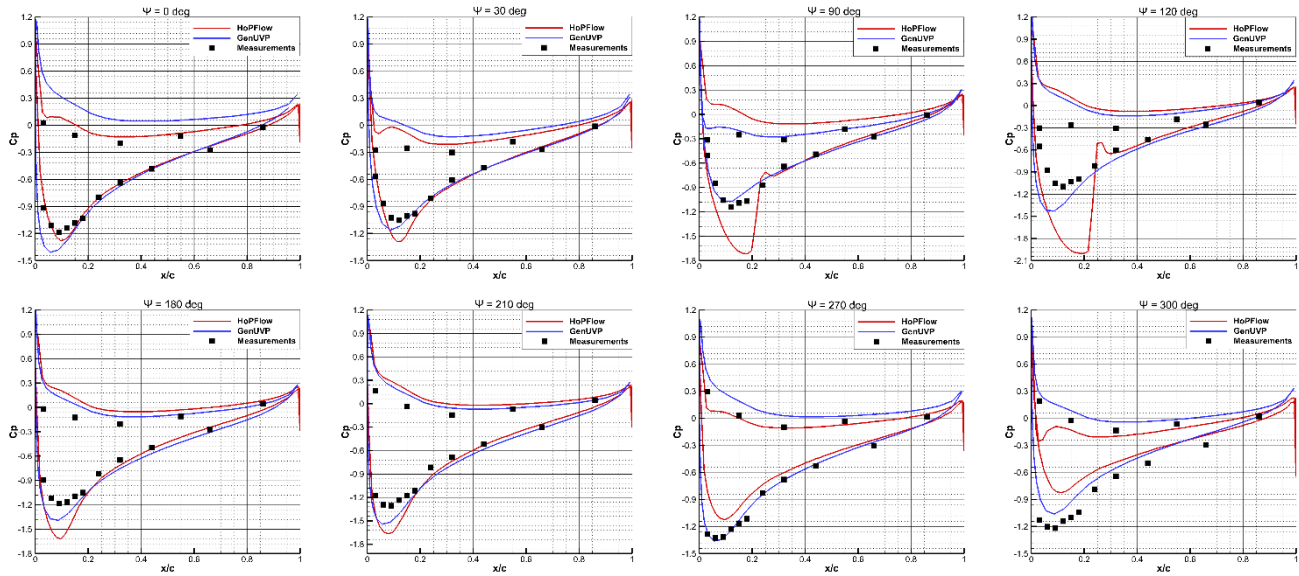


Figure 7: Pure aerodynamic simulations. Pressure distributions at $r/R=0.87$. BO105 in forward flight at 32.8m/s .

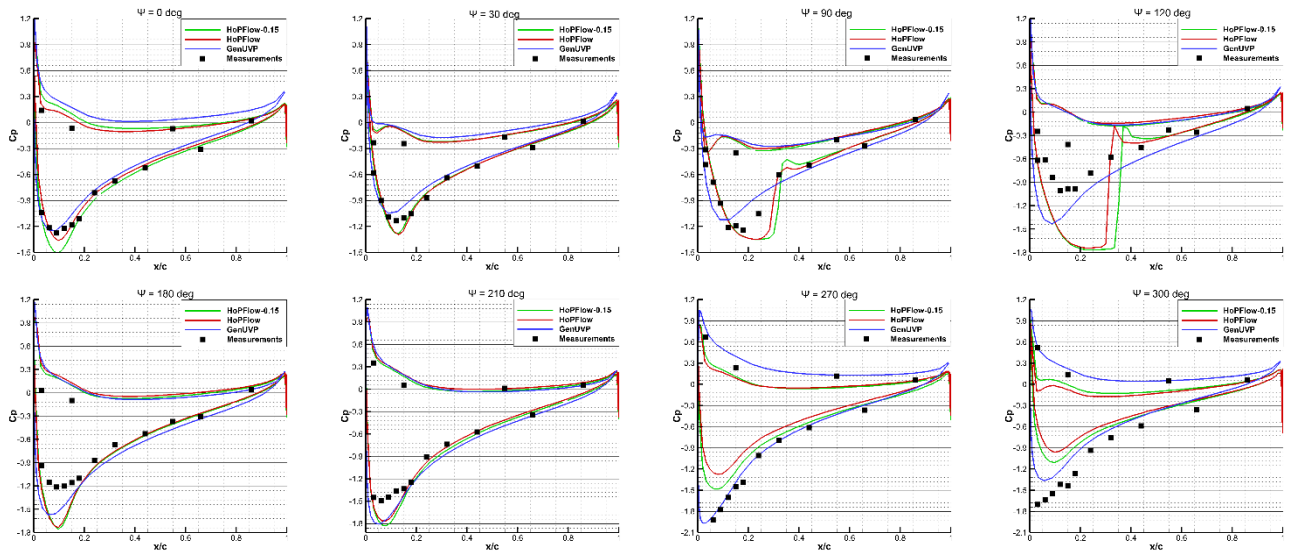


Figure 8: Pure aerodynamic simulations. Pressure distributions at $r/R=0.87$. BO105 in forward flight at 50.5m/s

This difference is mainly due to the level of angles of attack that the blade experiences. Over the

advancing side at 32.8m/s the higher angles of attack that as previously seen give rise to shock waves that

lead to higher flap moments. On the contrary over the retreating side the agreement is quite good. A similar behavior is seen also in the 50.5m/s case that is less intense due to the lower angles of attack that are formed. With respect to torsion moment, in both cases HoPFlow predicts lower values over the second half of the retreating side which is again attributed to the PM resolution.

3.2 Aeroelastic simulations

In this section results from fully coupled aeroelastic simulations are presented. When aeroelastic coupling is activated it is common practice to correct the loads provided by potential aerodynamic modelling. The usual way is to use look up tables in combination with a dynamic stall model. In this way viscous effects but most importantly Ma effects that are not included in the baseline flow solver, can be taken into account. In the GenUVP aeroelastic results this is done through the estimation of the effective angle of attack and effective relative inflow and the application of the ONERA dynamic stall model. Estimation of the effective conditions in CFD solvers, regardless whether they include or not viscous effects, is an open issue. In potential flow solvers, it is possible to isolate the conditions over a strip of the blade. In GenUVP the angle of attack is estimated from the total force while the effective relative velocity is calculated by excluding the self-

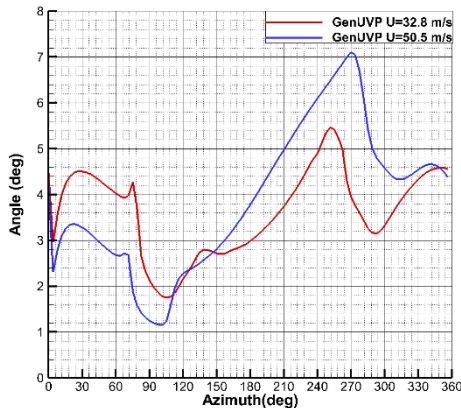


Figure 9: Pure aerodynamic simulations. Azimuth variation of the angle of attack at $r/R=0.87$ of the BO105 in forward flight, as estimated in the GenUVP simulations

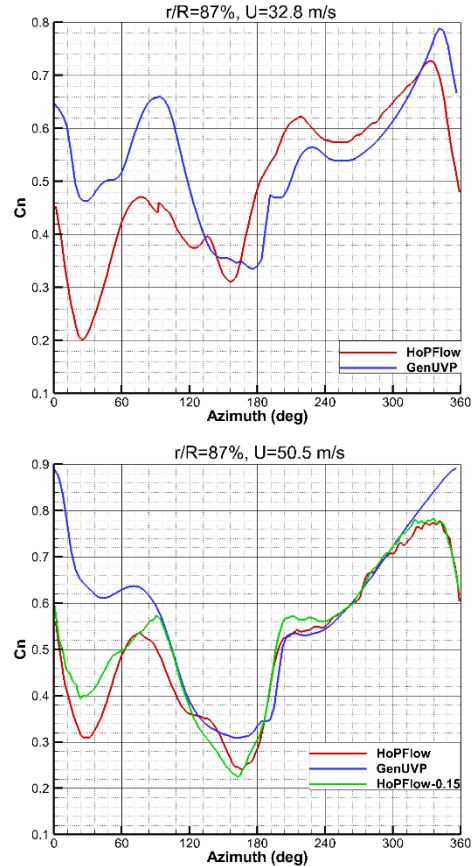


Figure 10: Pure aerodynamic simulations. Azimuth variation of the normal force coefficient at $r/R=0.87$ of the BO105 in forward flight at 32.8m/s (upper) and 50.5m/s (lower).

induced effect of the strip. In CFD such an “isolation” for the inflow conditions per strip is not straightforward. So, for the present simulations with HoPFlow the aerodynamic loads have not been corrected.

Another important aspect in aeroelastic simulations concerns the trimming. As already mentioned the values in Table 1 and the ones defined during the tests by the pilot so that the hub loads correspond to flight tests. Due to uncertainties in the model definition and the difficulty in exactly simulating the test conditions, the usual practice is to re-trim the control angles [16]. This process requires several revolutions until convergence is reached. In the present work, the rotor was not trimmed due to time constraints and limitations in the available computer resources. For consistency with the pure aerodynamic simulations, the measured trim was also used here.

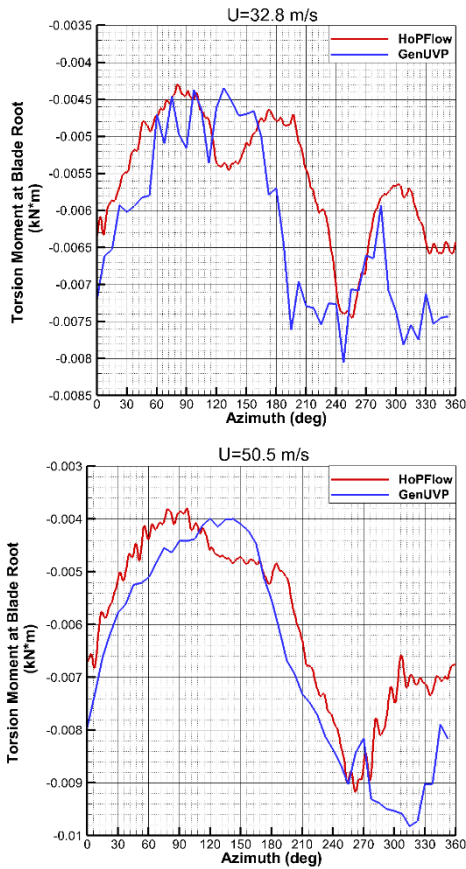


Figure 11: Pure aerodynamic simulations. Azimuth variation of the resulting torsion moment at blade root for the BO105 in forward flight at 32.8m/s (upper) and 50.5m/s (lower).

Pressure results for the two cases considered are given in Figure 13 and Figure 14. In the 32.8m/s case the effect of blade flexibility is clearly seen. The shocks that appeared in the purely aerodynamic simulations disappeared. The aerodynamic moment in the torsional direction is negative resulting in lower angles of attack. The two simulations compare well over the majority of the rotor disk. Only within the second half of the retreating side there is important difference. The HoPFlow predictions underestimate the loads which is due to the poor PM spacing. In comparison to measured tests, predictions show acceptable agreement. The differences are such that can be minimized with proper trimming.

Similar quality of results is also obtained in the 50.5m/s case. It is worth noticing that at all positions, the HoPFlow predictions give lower loading. This is due to the higher aerodynamic pitching moment that is calculated. It is reminded that the GenUVP predictions are based on an aeroelastic coupling that

makes use of the ONERA modelling while in the HoPFlow simulations the inviscid calculations are used directly. This results in higher negative moments which lead to higher torsional angles and by that to lower angles of attack as also indicated in Figure 16.

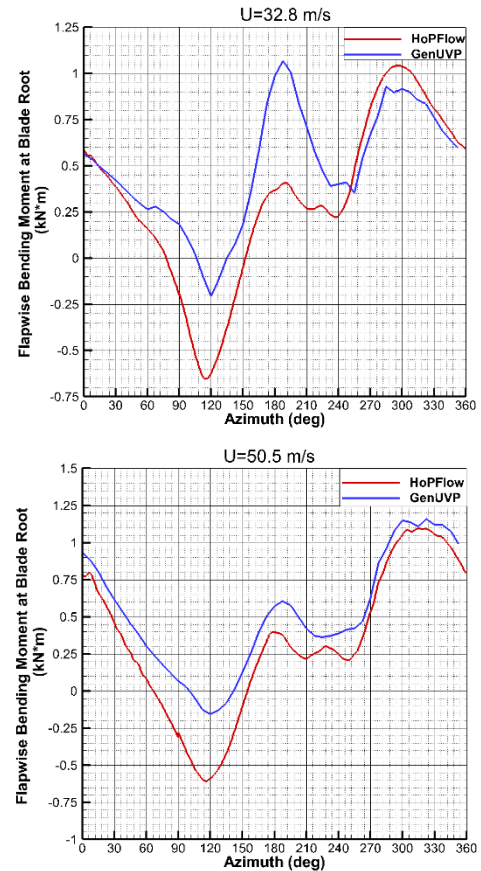


Figure 12: Pure aerodynamic simulations. Azimuth variation of the resulting flapping moment at blade root for the BO105 in forward flight at 32.8m/s (upper) and 50.5m/s (lower).

In Figure 15 results in terms of normal force coefficients are given from the GenUVP simulations. For the 50.5m/s case results with a lower by 1deg lateral cyclic value is provided. The shape and the level is similar to the one obtained in the tests for a slightly higher speed at 60m/s [17]. In Figure 17 and Figure 18 the azimuth variation of the main loads at blade root are provided. In the flapwise bending moment results at 50.5m/s, comparison to measurements are also shown. It is clear that by reducing the lateral cyclic value better correlation to the measurements is obtained. An important effect of the trimming is also seen in the variations of the torsional moment (Figure 18).

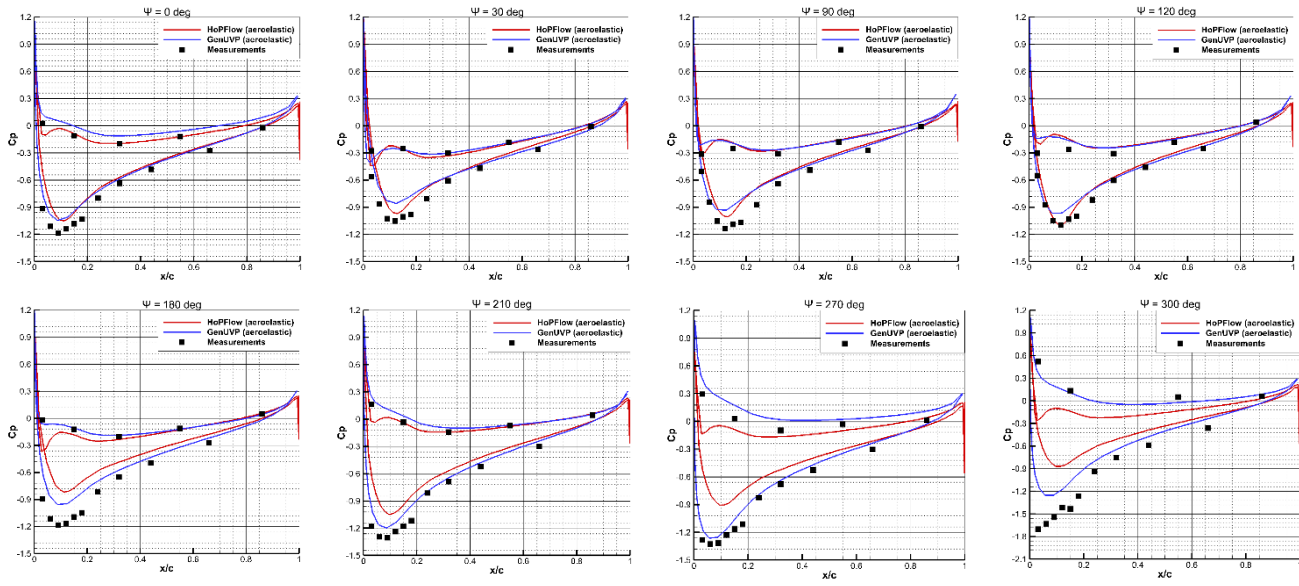


Figure 13: Aeroelastic simulations. Pressure distributions at $r/R=0.87$. BO105 in forward flight at 32.8m/s

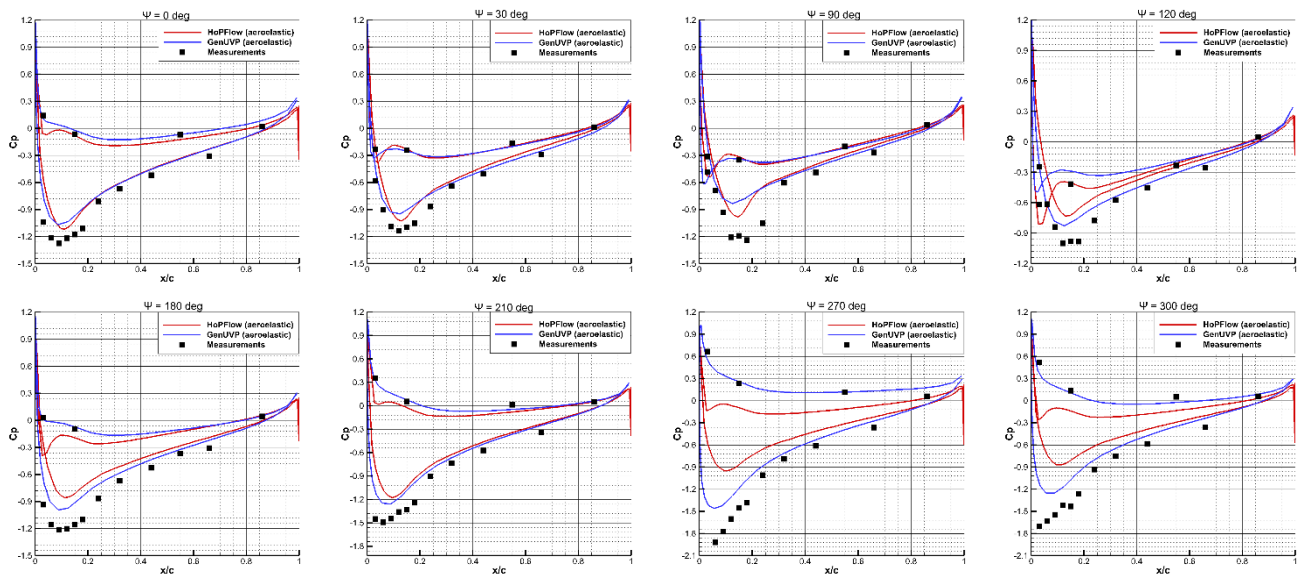


Figure 14: Aeroelastic simulations. Pressure distributions at $r/R=0.87$. BO105 in forward flight at 50.5m/s

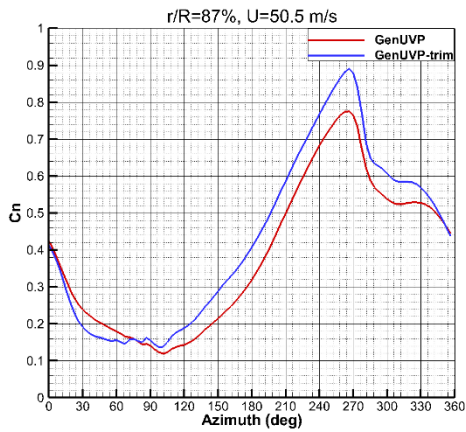
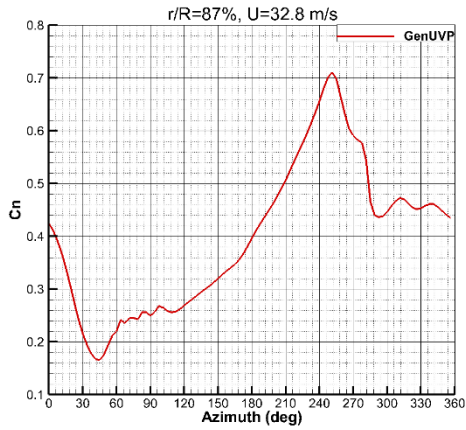


Figure 15: Aeroelastic simulations. Azimuth variation of the normal force coefficient at $r/R=0.87$ of the BO105 in forward flight at 32.8m/s (upper) and 50.5m/s (lower).

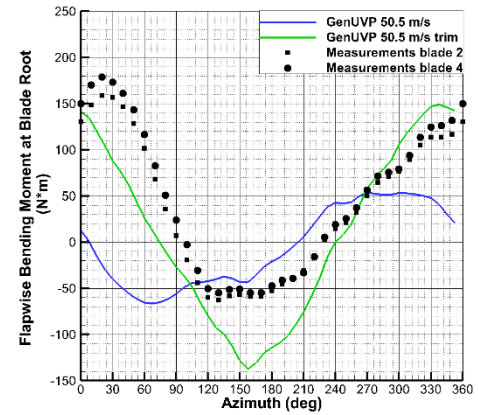
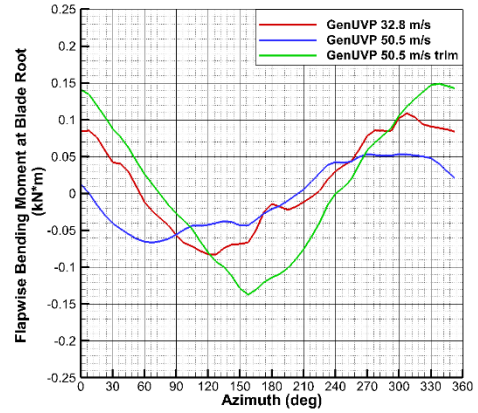


Figure 17: Aeroelastic simulations. Azimuth variation of the resulting flap bending moment at blade root for the BO105 in forward flight at 32.8m/s and 50.5m/s (upper) and comparison with experimental data (lower).

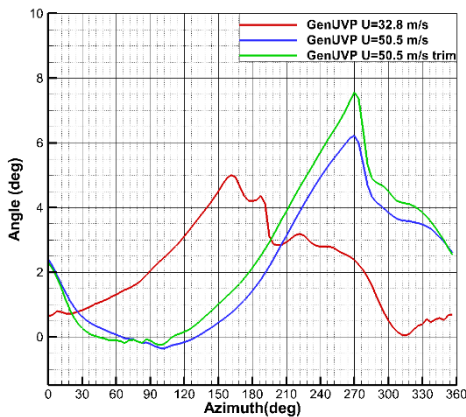


Figure 16: Aeroelastic simulations. Azimuth variation of the angle of attack at $r/R=0.87$ of the BO105 in forward flight, as estimated in the GenUVP simulations

4 DISCUSSION and CONCLUSIONS

A hybrid aerodynamic model (HoPFlow) has been presented which was coupled to a multi-body structural model for helicopter applications. Pure aerodynamic as well as fully coupled aeroelastic simulations of two forward flight cases for the BO105 helicopter have been conducted and compared to measurements. These results have been supplemented with similar ones obtained with an incompressible vortex flow solver (GenUVP) which was originally used in its thin wind version in the HeliNoVi project [17] while here is used in its thick wing version.

With reference to the pure aerodynamic simulations, it was found that the hybrid solver can provide meaningful results. In this respect, the quality of the predictions was found to depend on the PM grid spacing. In hover conditions, a spacing of $0.2c$ was sufficient while in forward flight a significantly smaller

value was necessary. Even the spacing of $0.15c$ was not found sufficient to properly simulate the flow over the last quadrant of the rotation. Besides this sector of the rotor disk, the rest was found consistent. On the other hand, the pure particle solver was found to be robust having however the disadvantage of being incompressible and therefore incapable of predicting shock waves – and compressibility effects in general.

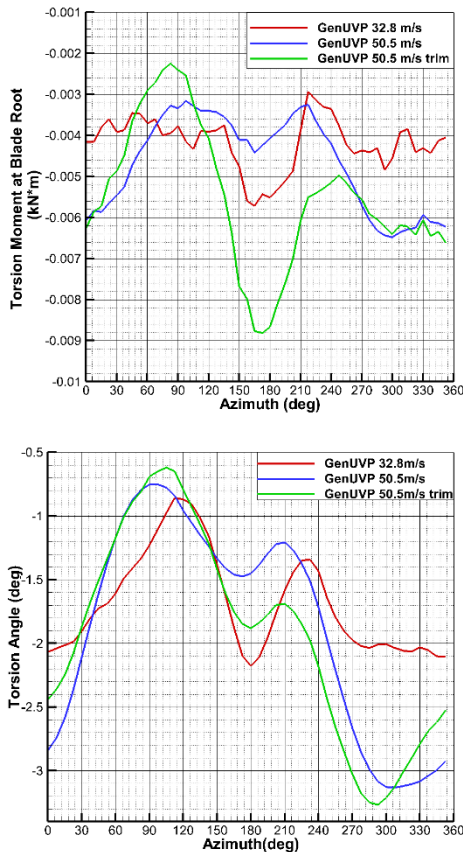


Figure 18: Aeroelastic simulations. Azimuth variation of the resulting torsion moment at blade root for the BO105 in forward flight at 32.8m/s (upper) and 50.5m/s (lower)

With respect to the aeroelastic simulations, on one hand the two sets of simulations were found in better agreement. This is due to the torsion angle that reduces the angles of attack and therefore limits the effect of compressibility. Both solvers converged to periodic states in approximately 5 full revolutions. The cost of such an aeroelastic simulation with HoPFlow is equivalent to 2000 core hours. It should be noted that trimming was not carried out and therefore the specific estimate of cost is too

optimistic. Depending on the flight conditions trimming may require a significant number of full rotations.

In conclusion, the results presented are regarded promising. In order to further reduce the PM spacing would require some modifications in the parallelization of the code in order to have good scalability. Then it is expected that accuracy will improve and the cost will be affordable to allow the trimming of the rotor.

Acknowledgements

This work was supported by computational time granted from the Greek Research & Technology Network (GRNET) in the National HPC facility - ARIS - under project "WINDAERO" with ID pr003028.

References

- [1] Quarteroni A and Valli A 1999 Domain decomposition methods for partial differential equations (Oxford Science Publications)
- [2] Cottet G H and Koumoutsakos P 2000 Vortex methods: Theory and Practice (Cambridge University Press)
- [3] Richardson S and Cornish A 1977 J. of Fluid Mechanics 82 309
- [4] Barba L, Leonard A and Allen C 2005 Int. J. Numerical Methods in Fluids 47 387
- [5] Koumoutsakos P and Leonard A 1995 Fluid Mechanics 296 1
- [6] Papadakis, G., & Voutsinas, S. G. (2014). In view of accelerating CFD simulations through coupling with vortex particle approximations. In Journal of Physics: Conference Series (Vol. 524, No. 1, p. 012126). IOP Publishing.
- [7] Voutsinas, S. G. (2006). Vortex methods in aeronautics: how to make things work. International Journal of Computational Fluid Dynamics, 20(1), 3-18
- [8] Colela G. T. Balls, P. Colella, A Finite Difference Domain Decomposition Method Using Local Corrections for the Solution of Poisson Equation, J. Computational Physics 180 (2002) 25.
- [9] Manolas, D. I., Riziotis, V. A., & Voutsinas, S. G. (2015). Assessing the importance of geometric nonlinear effects in the prediction of wind turbine blade loads. Journal of Computational and Nonlinear Dynamics, 10(4), 041008.

- [10] Anusonti-Inthra, Phuriwat and Floros M 2008 38th AIAA Fluid Dynamics Conference and Exhibit.
- [11] Stone C P, Duque E P, Hennes C C and Gharakhani A 2010 AIAA Paper 312
- [12] Boisvert, R. F. (1984). A fourth-order accurate fast direct method for the Helmholtz equation. *Elliptic Problem Solvers II*, 35-44
- [13] Huberson, Serge G., and Spyros G. Voutsinas. "Particles and grid." *Computers & fluids* 31, no. 4 (2002): 607-625.
- [14] Caradonna, F. X., and Chee Tung. "Experimental and analytical studies of a model helicopter rotor in hover." (1981).
- [15] H.-J. Langer, O. Dieterich, S. Oerlemans, O. Schneider, B. Van der Wall, J. Yin, "The EU HeliNOVI Project - Wind Tunnel Investigations for Noise and Vibration Reduction", 31st European Rotorcraft Forum, Florence, Italy, September 13-15, 2005.
- [16] V.A. Riziotis, SG Voutsinas (2006) "Modelling of wind tunnel interference on helicopter measurements and assessment of the currently used corrections based on the HeliNovi data base" 32nd European Rotorcraft Forum, Maastricht, The Netherlands
- [17] A. Visingardi, A. Dummel, D. Falchero, M.Pidd, SG Voutsinas, J. Yin (2006) "Aerodynamic interference in full helicopter configurations: validation using the HeliNovi database" 32nd European Rotorcraft Forum, Maastricht, The Netherlands.